an experimental measurement of the combined brehmmstrahlung and the ionization loss. At the three main field settings, 6.6, 5.3, and 4.4, checks were made of the electronics to measure accidental rates. Approximately 2 x 10^5 events of this type were recorded.

IV. SONIC SPARK CHAMBERS AND SOUND RANGING

A. Theory of Operation

When a spark chamber is pulsed and breakdown occurs, not only is a spark visible but there is a sound wave which can be detected by a microphone. The time interval from the instant the spark is generated until the instant the sound of the spark is detected by a microphone is almost proportional to the distance between the spark and microphone. The speed of sound in neon, the gas usually used for spark chambers, is 0.5 mm/μsec. To measure a distance of 50 cm to 0.5 mm it is necessary to measure 1 msec to 1 μsec. In practice with standard electronics time resolutions of 0.050 μsec are achieved easily. The accuracy of this measurement is limited by the risetime of the microphone pulse and the acoustical wave, both of which are of the order of 1 μsec.

The first experimentalists to use the sound of the spark to measure position were Fulbright and Kohler of Rochester University.[22] Independent of this work Kirsten and Maglic devised a sonic spark chamber and demonstrated the feasibility of using it in a high rate experiment.[23] On the basis of the success of these devices, a sonic spark chamber was built at the Nevis Laboratories in September 1962. The Nevis chambers

are single-gap spark chambers with four microphones mounted inside the chambers. An assembled chamber, shown in Fig. 10, consists of a rectangular brass frame to which thin foil electrodes are attached. The microphones are held in brass brackets which are in turn mounted on the inside walls of the frame.

The microphones form a rectangle of sides 2a and 2b, as shown in Fig. 17. The most natural set of coordinates to describe the location of a particle track are the perpendicular bisectors of the sides of the rectangle. The intersection of the bisectors is the origin. The x coordinate axis is parallel to the side formed by microphones 1 and 3, and the y coordinate axis is parallel to the side formed by microphones 1 and 2.

ARRANGEMENT OF MICROPHONES IN A SONIC CHAMBER

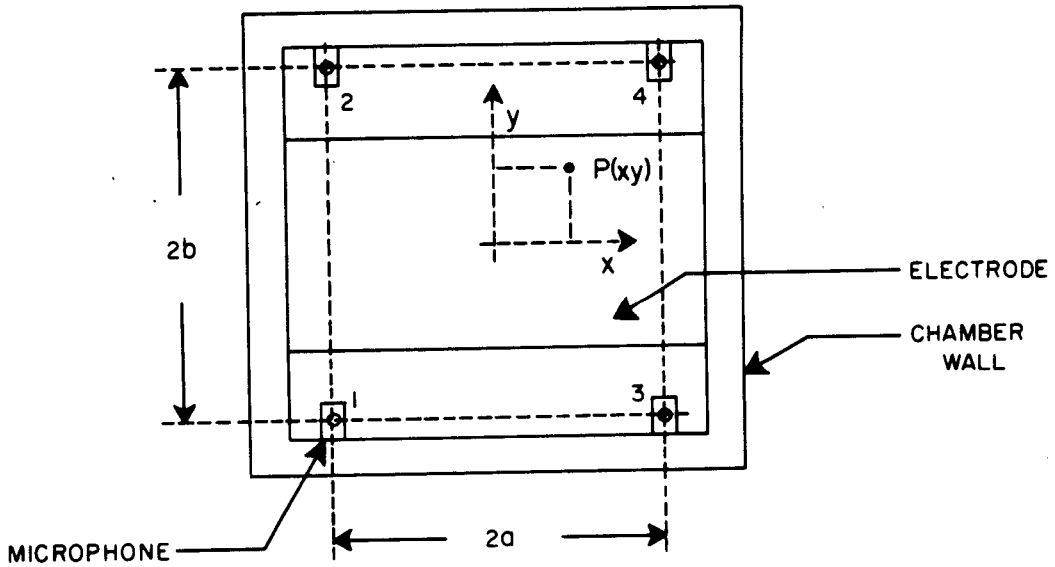

FIG.17

Fig. 17 Arrangement of Microphones in a Sonic Chamber

The relationship between the distance traveled by the sound wave and the time of propagation is given approximately by

$$d = Vt + K \tag{10}$$

d is the distance between the microphone and the spark; V is the velocity of sound in the gas; t is transit time of the soundwave between spark and the microphone; and K is a constant which accounts for the fact that during the first centimeter of travel the speed of the disturbance is greater than V.

When the spark is generated the average kinetic energy of the particles is much greater than the average kinetic energy of the particles in the remainder of the gas. Since the electrical discharge lasts for a time which is less than 250 nsec, the particles in the gas do not diffuse outward during the discharge and their density is the same as the bulk gas. If the average kinetic energy per particle in the spark is kT_S and the average kinetic energy per particle in the gas is kT_O, then the pressure difference at the time of the formation of the spark is

$$(P_S - P_O) = \rho Nk(T_S - T_O) \quad . \tag{11}$$

The disturbance will be approximately cylindrical. If the energy in the disturbance is considered to be constant, then as the disturbance spreads out the pressure decreases. If $P_S(r)$ is the pressure in the disturbance after it has spread out a distance r and if the energy density within the disturbance is uniform, then $P_S(r)$ is given by

$$P_S(r) - P_O = \rho Nk(T_S - T_O)\frac{c^2}{r^2} \quad . \tag{12}$$

c is the radius of the spark after the electrical discharge stopped. As long as the excess pressure is large the disturbance will be propagated with a velocity greater than the speed of sound. Once the excess becomes relatively small, that is $\left(\frac{T_S - T_O}{T_O}\right) \frac{c^2}{r^2} < 1$, the disturbance will be propagated with speed of sound. The distance K at which this is true is given by

$$K \approx \left(\sqrt{\frac{T_S - T_O}{T_O}}\right) c \approx \sqrt{\frac{f(C_D V_D^2)}{kT_O}}$$

If c is taken to be 1 mm, the typical width of a spark on a photograph and if T_S is about 1 eV, the value of K will be about 1 cm. It is of importance to note that the disturbance propagates with the speed of sound after 1 cm or so. From Eq. (13) it can be seen that K varies as the square root of the kinetic energy of the particles in the discharge. The kinetic energy of the discharge depends in turn on the energy stored in the discharge capacitor, $1/2(C_D V^2)$. While the energy dissipated in the spark is not a constant fraction of the energy stored in the discharge capacitor, it does depend only on the voltage to which the capacitor is charged, the capacitance, and the time response of the high-voltage trigger circuit. As long as these quantities are kept constant, K can be kept constant. In practice the charging voltage was kept constant to a few percent. An equivalent form of Eq. (10) is

$$d_i = V(t_i + t_p) \quad .$$

t_i is the time interval which was measured for the i^{th} microphone. The time interval, which begins 60 μsec after the

spark chambers are pulsed, is measured by scaling a 5-Mc oscillator. The relationship between t_p and K is further modified by the finite size of the detector. The relation between K and t_p is given by

$$t_p = 300 + \frac{K + R_d}{V} \quad \text{(units of 1/5 } \mu\text{sec)} \tag{15}$$

R_d = radius of the lead zirconate cylinder .

The times measured by the acoustic pickups are related to the location of the spark by Eqs. (16) and (17).

$$x = \frac{V^2}{4a}\left[(t_1+ t_p)^2 - (t_3+ t_p)^2\right] = \frac{V^2}{4a}\left[(t_2+ t_p)^2 - (t_4+ t_p)^2\right] \tag{16}$$

$$y = \frac{V^2}{4b}\left[(t_1+ t_p)^2 - (t_2+ t_p)^2\right] = \frac{V^2}{4b}\left[(t_3+ t_p)^2 - (t_4+ t_p)^2\right] \tag{17}$$

Both x and y can be determined in two ways. The quantity DT, defined by Eq. (18), is zero for a single spark. It is therefore a test of the consistency of the measurement and an indication of whether more than two sparks are in the chamber.

$$DT = (t_1+ t_p)^2 - (t_2+ t_p)^2 - (t_3+ t_p)^2 + (t_4+ t_p)^2 \tag{18}$$

A second consistency check is given by the null quantity D:

$$D = (a + x)^2 + (b + y)^2 - V^2(t_1 + t_p)^2 \tag{19}$$

Using four microphones makes it possible to detect double sparks. DT is a good check on whether all transducers are working and it does not depend on V. D is then a check on V and, in addition, removes the few ambiguities which can occur in the DT check. For sparks near a microphone, DT is

very sensitive to t_p; and thus t_p is determined from the experimental data by choosing a sample of these points, setti DT = 0, and then solving for t_p. Throughout the experiment t_p is checked for data samples. Since its variation is withi the statistics of a single sample, one set of values is used for the data analysis. In a similar way, V is sensitive to points in the center of the chamber and it is checked in this manner.

The velocity of sound V is not a constant. V must be redetermined from time to time, for it cannot be controlled as is the case with t_p. The gas used in the chamber is a mixture of He and Ne which obeys the ideal gas law. The velocity of sound in an ideal gas is expressed by

$$V^2 = (\gamma R) \frac{T}{M} \quad . \qquad (2$$

γ is the ratio of specific heats and R the ideal gas constant, T is the gas temperature and $\bar{M}$ the mean molecular weight. A 3^{o} C change in T, which is not uncommon, will produce a 1% cha in V^2. Such a change must be accounted for if the position of a spark is to be determined within 1/2 mm. The mean molecul weight can also change because the Mylar windows are more poro to He than Ne. The change in $\bar{M}$ is of more significance in practice than the change in T.

The velocity of sound is determined by a test spark, a pair of needles which are located at a fixed position, as shown in Fig. 16. If a large voltage is put across the needle a spark will be made and the velocity can be determined by

$$V = \left(\frac{d_3 - d_1}{t_3 - t_1} \right) \quad . \tag{21}$$

The advantage of using the test spark to determine V rather than the data from a real spark is that the test spark can be placed so that it is sensitive to V, while the real sparks occur throughout the chamber. In practice this relation was not used directly to get V, but it was related to an optical calibration.

B. Calibration of the Chambers and Bench Tests

The first check of accuracy of the spark chamber compares the position of the spark measured from photographs to the same position measured by the microphones. The relations used to compute the position are,

$$x = \frac{V^2}{4a} \left[\frac{(t_1+t_p)^2 - (t_3+t_p)^2 + (t_2+t_p) - (t_4+t_p)^2}{2} \right] \tag{22}$$

$$y = \frac{V^2}{4b} \left[\frac{(t_1+t_p)^2 - (t_2+t_p)^2 + (t_3+t_p)^2 - (t_4+t_p)^2}{2} \right] \tag{23}$$

X_{op}, the X coordinate of the spark as determined from the photograph, and X_a, the sonic measurement, are fitted by least squares to a relationship of the form:

$$X_a = \alpha X_{op} + \Delta X_{op} \quad . \tag{24}$$

X_{op} is measured from a fiducial mark on the spark chamber. ΔX_{op} is the distance from the optical fiducial mark to the center of the chamber. X_a is determined from the sonic times using Eq. (22) when $V^2/4a$ is set equal to 1. It is possible to fit the points (X_a, X_{op}) to a straight line by Eq. (24)

to an accuracy of 0.2 mm. The slope of this straight line, α, is $4a/V^2$ and hence determines V^2. V^2 can also be determined by an independent measurement which uses the test spark. According to Eq. (21), while the value of V^2 determined by the two methods differs by 1/2%, the ratio of the two measurements is almost independent of the value of V^2. A factor of two-change in V^2 changes the ratio by 3%. For normal conditio V^2 changes only by 10%. Over this range the ratio of the two methods for determining V^2 will be constant to 1 part in 1000. As a consequence, it is possible to determine the appropriate value of V^2 to use in Eqs. (22) and (23), by knowing the value of V^2 from the test spark and the ratio of the two values of V^2. In practice this is done by evaluating the quantity λ, defined by Eq. (25), which is proportional to the ratio of V^2 as determined from the two methods.

$$\lambda = \left(\frac{V^2}{4a}\right) \frac{}{(t_1 - t_3)^2_{TS}} \qquad (25$$

$\overline{(t_1 - t_3)}_{TS}$ is the average value of the difference in time for microphones 1 and 3 when the test spark is fired. By combining Eq. (24) with Eq. (21), it follows that λ should be equal to Eq. (26) and independent of V^2:

$$\lambda = \frac{(d_1 - d_3)^2}{4a} \qquad (26$$

Once the constant λ has been determined, the value of $V^2/4a$ can be obtained by continually monitoring the value of $\overline{(t_1 - t_3)}_{TS}$. By repeating the optical calibration for a wide variation of the amount of He in the He-Ne gas mixture in the

spark chamber, it is possible to change V^2 by a factor of 2. The values of $V^2/4a$ and λ are determined for each gas mixture by an optical calibration. t_p is measured by using Eq. (18) with DT set equal to zero. By choosing sparks only near the microphone, t_p can be measured quite well. The practice determines t_p for each optical calibration. The results of these calibrations are presented in Table III.

TABLE III

Bench Tests of 14 in. x 10 in. Sonic Spark Chambers
August 1963

Run No.	Chamber I		Chamber II		Chamber III	
	$V^2/4a$	λ	$V^2/4a$	λ	$V^2/4a$	λ
1	0.826	0.444	0.522	0.445	0.515	0.452
2	0.920	0.444	0.546	0.446	0.510	0.452
3	0.517	0.460	0.607	0.445	0.578	0.449
4	0.512	0.461	0.517	0.444	0.515	0.452

The data show that λ varies very slowly with V^2. In the course of the experiment the extreme variation of V^2 was about 10%. Over this range of V^2, λ can be considered to be a constant. These tests demonstrate that the chambers could locate a spark to 0.2 mm when calibrated with optical measurements. Moreover, by determining λ the V^2 of the spark chamber could be determined as a function of test spark times. The systematic error due to the slight variation of t_p with distance, and other such errors are eliminated to first order by the calibration procedure.

A second set of bench tests was performed by arranging the four chambers one on top of the other in an Aℓ frame machined by 0.001 in. A photograph of the setup which shows the sparks due to a β from Y_r^{90} decay is shown in Fig. 18. Approximately 100 pictures were taken and measured. The absolute location of the x coordinate was referenced to fiducial marks on the Aℓ frame.

TABLE IV

Bench Tests of the Sonic Chambers Used in the Experiment
April 1964

Chamber	t_p	$V^2 \times 10^5$ (cm^2/t^2)	ΔX_{op} by Machinists Measurements (in.)	ΔX by Calibration (in.)
I	370	8.774	0.037	0.036
II	375	8.936	0.069	0.071
III	380	8.915	0.069	0.066
IV	380	8.921	0.099	0.097

The location of the center of the spark chamber is not dependent on V or t_p, but depends only on the location of the microphones. These were mounted in brackets, an example of which is shown in Fig. 19. The microphone is held in place in the bracket by a rubber O-ring. The bracket itself is pinned accurately to the frame. The location of the center of the chamber, ΔX_{op}, was computed from the bracket locations. These locations were given on the basis of the machinists' measurements of the mounting holes. The data show that there was no slip of the microphones in the O-rings, as the relative

positions of the centers from one chamber to another agree to within 0.005 in. The absolute location deviation reflects the accuracy of the optical system. These comparisons indicate how well sparks in separate chambers were measured relative to one another in the experiment.

To check how well the calibrated sonic chamber worked, a separate experiment was carried out using cosmic rays. The chambers were arranged as shown in Fig. 20. Cosmic rays passing through the chamber were detected by scintillation counters. In order to minimize multiple scattering in the spark chambers only cosmic rays which had penetrated 7-in. lead were used to trigger the chambers. This set a cutoff of 250 MeV/c in momentum. The quantity ΔX defined by Eq. (27)

$$\Delta x = \frac{(X_I - X_{III}) - 2(X_I - X_{II})}{2} \tag{27}$$

is the deviation of the spark in Chamber II from a straight line through the sparks in Chambers I and III. Because multiple scattering is neglible, the deviation can only depend on the sonic measurement error. The positions were computed using $V^2/4a$ and $V^2/4b$, which correspond to the times measured by the test spark. $(\overline{\Delta x^2})^{1/2}$ was found to be 0.3 mm. Figure 21 shows a histogram of Δx. The width of this distribution depends only on the accuracy of the spark chambers and hence is a measure of the accuracy of each chamber. It reflects the cumulative error of the single measurement, the test spark, and the calibration. It is not a fitted result.

The data of Table V obtained by photographing the chamber in the magnet during the experiment, provided the calibration for the data obtained in the experiment. It represents the most extensive calibration carried out as 300 pictures were taken and measured. The value of σ is poorer only because the camera was much further away than in the bench tests.

TABLE V

Experimental Calibration

July 1964

	Chamber I			Chamber II		
Run	$V^2 x 10^3$ (mm/unit t)^2	λ (mm)^2	σ mm	$V^2 x 10^3$ (mm/unit t)^2	λ (mm)^2	σ mm
9902	8.88	4367	0.23	8.88	45930	0.30
9904	8.87	4346	0.25	8.89	45910	0.27
9906	8.91	4360	0.27	8.89	45870	0.23
9913	9.21	4361	0.27	9.13	45710	0.27
9916	9.22	4372	0.27	9.14	45840	0.23
9921	9.75	4389	0.32	9.65	45849	0.23
	Chamber III			Chamber IV		
9902	8.85	45070	0.27	8.80	20130	0.25
9904	8.86	45050	0.30	8.81	20130	0.15
9906	8.87	45090	0.20	8.81	20130	0.25
9913	9.11	44970	0.32	9.09	20120	0.23
9916	9.12	45050	0.32	9.13	20290	0.23
9921	9.59	44976	0.27	9.57	20230	0.23

V is the velocity in mm/0.2 μsec, λ is a constant, σ is the standard deviation of the fit of a straight line to optical and sonic measurement.

C. Description of a Typical Chamber

The sonic chamber is a one-gap spark chamber with four microphones mounted on the walls inside the chamber. The microphones are cylindrical shells of lead zirconate which are silvered inside and out. The outside diameter is 1/8 in., the inside diameter 1/16 in., and the length 1/2 in. The cylinder, together with a brass cap and fitting, is soldered to a piece of thin coaxial cable. The coaxial mounting reduces the pickup of the spark discharge to tolerable levels. The brass cap and fitting are grooved so that a small rubber O-ring may be slipped on. A photograph of a microphone, its cable, and the mounting fitting is shown in Fig. 19. The microphone is held in position in a brass bracket mounted on the wall of the chamber. The brackets are held in place by nylon screws, which provide support and shock isolation. The spatial location of the bracket is determined by a milled slot into which the bracket slips.

The screws and rubber O-rings effectively isolate the microphone from wall vibrations. The microphone signals are brought out of the chamber by coaxial feed-throughs mounted on the front wall. Also mounted on the front wall are two valves which permit gas to be circulated through the chamber.

The electrodes of the spark chamber are 0.001-in Al foil stretched on stainless steel frames. The windows of the chambers are 0.003-in. Mylar. All seals are made with O-rings. The chambers are leaktight to freon leak detectors, although He will diffuse through the windows. The test spark, a pair

of tungsten electrodes mounted on a lucite bracket, is attached to the inside wall.

The brass frame of the chamber was machined to 0.001 in. tolerances. The microphone bracket holes were drilled after the brackets were in place, so that the centers of the holes would be positioned to ± 0.001 in. The use of rubber O-rings to position the microphone reduces the precision of the mountin somewhat, but the error introduced is less than 0.005 in. The important dimensions of the chambers used in the experiment are given in Table VI.

TABLE VI

Spark Chamber Dimensions

Chamber	Plate Area (in.)	2a (cm)	2b (cm)
I	$5\frac{1}{2}$ x $5\frac{1}{2}$	14.290	21.433
II	14 x 10	34.290	35.687
III	14 x $11\frac{1}{2}$	34.290	36.195
IV	12 x 12	29.210	41.275

D. Sonic Spark Chamber Electronics

The sonic data system measured the transit times of the soundwave to the microphones, converted the measurements to digital form, and wrote the digital data on tape. The hardware is composed of two parts, an IBM 1401 computer and a sonic data unit. The sonic data unit was designed and made at Nevis. A description of its operation is given in this section, with a number of details placed in Appendix III.

The time intervals between the generation of a spark and the arrival of the soundwave at the four microphones were measured and written on magnetic tape by the following sequence of operations:

1) After a delay of 60 μsec, a set of 5-Mc oscillators were gated on by the spark chamber trigger pulse and then gated off by the amplified microphone pulse.
2) During the time interval that each oscillator was gated on, it was scaled by a separate four-digit coded decimal scalar.
3) The digitized time intervals were transmitted to the 1401 memory one digit at a time. Transmission of digits to the 1401 was stopped after all time intervals were read.
4) The process was repeated until n such events have been read into the 1401 memory; then the data in the memory was written on magnetic tape as a single record. The number n was controlled by the 1401 program. (During the experiment n was 12.)

The block diagram of Fig. 21 shows schematically how each of the first three operations are carried out. The fourth operation is controlled by the 1401 and its program. The measurement of the time interval and its subsequent conversion from analog to digital form is done by the time interval channel. Data transmission to the 1401 memory is controlled by the main control chassis and the 1401 control chassis.

Aside from the microphone detector and its amplifier the electronics is typical of any 5-Mc saturated switching logic. The properties of the microphone and the amplifier were matched so that the system would be sensitive to only the soundwave and not extraneous vibrations.

The soundwave is detected by a lead zirconate cylindrical shell which generates a potential difference across the shell when it is struck by the soundwave. The output of a microphone, which is of the order of 1 mV, is amplified by a factor of 1000 and the amplified pulse is the digitron stop pulse. Figure 23 shows a transducer pulse after amplification. The 1-μsec rise of the pulse is due to the response of the high frequency vibration mode of 500 kc of the lead zirconate cylinder and the spatial definition of the soundwave. The ringing at 500 kc shows that this mode is excited directly by the sound wave. A second mode of vibration at 50 kc is set into vibration if the holding bracket is made to vibrate, and it is also set into vibration by the coupling between the two modes. The bracket will vibrate if a soundwave strikes the brass frame. This can be serious since a soundwave can strike the brass frame and then travel through the frame to the bracket. Because the speed of sound in brass is ten times greater than in neon, the soundwave can reach the microphone by this path before the soundwave in neon reaches the microphone. The amplifier is designed to pass the high frequency mode and reject the low frequency mode. The half-power points of the output are

roughly 100 kc and 2000 kc. A block diagram of the amplifier and time interval flip-flop is given in Fig. 24.

After the pulse has been amplified it is fed into one side of a differential amplifier which is biased by an exponentially decaying pulse. The output of the differential amplifier is used to reset a flip-flop which stops the 5-Mc oscillator. The purpose of the exponentially decaying pulse is twofold. First, it gates the discriminator off when the spark chamber is fired; and second, it provides a time-varying discrimination level, thus making it possible to stop the 5-Mc oscillator at the same point on the rise of the microphone pulse, irrespective of where it comes from in the chamber. The pulse height of the microphone pulse is a function of distance and varies inversely as $d(\exp \alpha d) \cdot \alpha \approx 1 \times 10^{-3}/\text{cm}$. A graph of the amplified microphone pulse height vs time is shown in Fig. 25.

Two milliseconds after the spark chambers are fired, data acquisition is complete and all 5-Mc clocks not stopped at this time are stopped by the disappearance of the amplifier gate pulse. In this experiment the largest possible transit time was less than 1 msec. The end of amplifier gate pulse starts the data-reading sequence which is shown in block diagram in Fig. 26. This pulse generates a service request which is sent to the 1401. If the 1401 is ready to read the data stored in the scalars of the sonic data unit, a read-call level is present and the sonic data unit puts the first digit on the five data lines to the 1401. These lines are an 8, 4, 2, 1, and a parity line. The 1401 reads these lines,

sends a clock pulse to the sonic data unit, and stops to await the next digit. The 1401 clock pulse moves the step sequence to the next position, thereby bringing the next digit on to the data lines. The 1401 clock pulse also gates the service request off for its duration, thereby providing the time in which to move the next digit onto the data lines. After the 1401 clock pulse is over a new service request is generated and the 1401 reads the data, generates a second clock pulse, and then stops to await the next digit. This sequence is repeated until the last digit has been transmitted. At this time the step sequence generates an end of transmission pulse which the 1401 recognizes, and permits it to carry out the next step in its stored program. Total time to acquire and read the data is 3.5 msec. The 1401 program used in this experiment carries out a series of computations between events which last 20 msec. A discussions of the operations carried out by the 1401 is given in Sec. VI, while finer details of the operation of the sonic system are given in Appendix II.

The advantage of the sonic spark chambers over conventional spark chambers which use optics and photography to determine spark positions is striking. An excellent optical system and excellent measuring can locate sparks to 0.25 mm in space, while the sonic system can locate sparks to 0.30 mm in space. The accuracy of each system is roughly equivalent. In the sonic system data can be put into a computer within 4 msec after the event occurs and it is ready to be processed; moreover, as soon as the chambers can be pulsed again it can

handle another event. Event rates of 60/sec were achieved using a β-source. The conventional system is limited by camera drive speeds to a few pictures a second.

V. CONSTRUCTION OF A THEORETICAL MUON DECAY SPECTRUM

A. The Choice of a Theoretical Model

The theoretical model to which the experimental results were compared is the four-fermion contact interaction given by Eq. (5). A consequence of Eq. (5) is that the decay spectrum can be described by a simple polynomial in the electron momentum as given by Eq. (9). For unpolarized muon decays this polynomial is characterized by only two parameters, ρ and η. The details of the interaction between the four fermions is contained in ρ and η. While the simple polynomial must be modified to include radiative corrections, it is still characterized by the parameters ρ and η. As long as the results of an experiment are presented in terms of ρ and η, the ordering of the lepton fields is immaterial. When an interpretation of a particular set of values of ρ and η is made in order to obtain limits on the fundamental coupling constants, the ordering of the lepton fields is crucial. For this reason the ordering can be ignored temporarily and will be until an interpretation of the experimentally determined values of ρ and η is made in Sec. VIII. The remainder of this section will be devoted to the modifications which must be made to Eq. (9).

Large non-local effects can be ignored because there is no evidence for their existence. Small non-local effects can be included into Eq. (9) as their dominant effect causes

small changes in ρ and η. A plausible means of introducing a non-locality is to couple the weak interaction current, J_α, to a massive spin 1 particle, W. The weak interaction lagrangian becomes

$$\mathcal{L} = g\, J_\alpha W^\alpha \qquad g = M_W \sqrt{G_f} \tag{28}$$

W^α is the vector field describing the boson and M_W its mass. In this case the observed weak interaction processes are all second order. A further consequence of the spin 1 particle is that it will have the effect of increasing the observed Michel parameter by the amount

$$\Delta\rho = \frac{1}{3}\left(\frac{M_\mu}{M_W}\right)^2 \simeq \frac{1}{3}\left(\frac{.1}{80}\right)^2 \simeq \frac{1}{3}\,\frac{10^{-2}}{6.4\,10^3} \tag{29}$$

The original motivation for the experiment described here was to detect the existence of that correction. Since the start of this experiment a number of other experiments have placed a lower limit on the mass between 2.0 and 4.0 BeV.[24,2] For such a lower limit on the mass the correction to ρ is less than 0.001, and thus beyond the accuracy of the experiment.

B. Internal Radiative Corrections

The modifications to Eq. (9) to account for the internal radiative corrections have been computed by using the minimal electromagnetic interaction which is known to be applicable to both the muon and electron.[1] These corrections to order α^2 are described by the following Feynman diagrams:

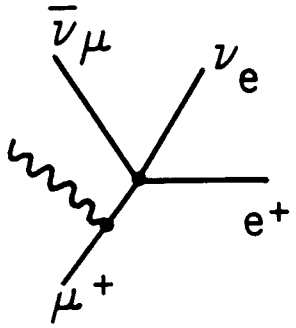

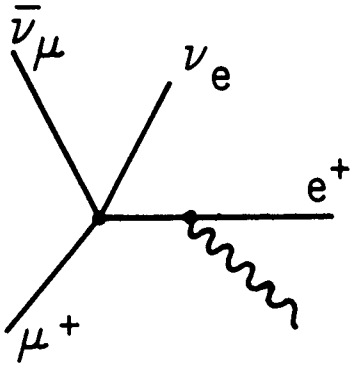

Diagrams A_1 and A_2 contribute because the apparatus does not distinguish the cases in which photons are emitted from the case in which they are not.

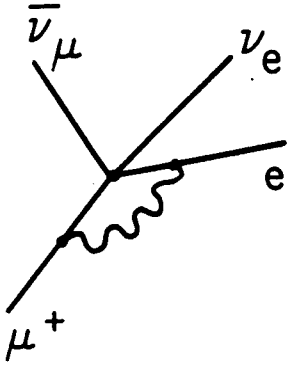

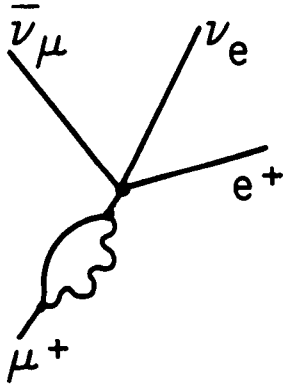

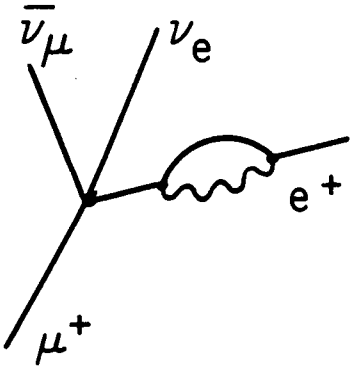

Diagram B_0 is the unmodified graph, while Diagram B_1 is the vertex modification, and B_2 and B_3 are the mass renormalization graphs.

The calculation can be carried out in a convergent manner in only one case, the case of V-A theory.[1] The calculation has also been done for the case of the intermediate boson. The difference between a local theory and a boson theory is small and varies as $(M_\mu/M_W)^2$.[26] For other types of coupling the results are divergent. For a cutoff of M_p the results are roughly independent of the exact nature of the weak vertex. As a V-A theory is at least correct to 1%, the radiative corrections for this theory were used. The results modify the spectrum in the following manner:

$$\frac{dN}{dx} = x^2\left\{\left(\frac{1}{1+\frac{4m_e}{m_\mu}\eta}\right)\left[3(x-1)+2\rho\left(\frac{4}{3}x-1\right)+6\frac{m_e}{m_\mu}\eta\left(\frac{1-x}{x}\right)+\frac{\alpha}{2\pi}f(x)\right]\right. \quad (3$$

$$\left. - \xi p\cos\theta\left[1-x+2\delta\left(\frac{4}{3}x-1\right)+\frac{\alpha}{8\pi}g(x)\right]\right\}$$

$\frac{\alpha}{2\pi}f(x)$ and $\frac{\alpha}{2\pi}g(x)$ are integrals which give corrections of a few percent throughout the spectrum, except at $x = 1$ where they are divergent. The difficulty arises from the fact that the S-matrix for μ decay has been expanded in terms of one emitted photon, two emitted photons, etc.

The divergence can be overcome formally by including an experimental resolution which allows the integrals for $f(x)$ and $g(x)$ to converge. The inner bremsstrahlung process, the sum of diagrams A_1 and A_2, has been checked experimentally and is in agreement with the V-A theory to the accuracy of the experiment.[27]

The use of radiative corrections for a pure V-A theory, while retaining a spectrum which was derived from a more general hamiltonian, is a questionable procedure. The justification for this approach is due in part to the fact that the radiative corrections are not sensitive to the exact form of the interaction, and in part to the historical precedence that this means of reporting the data has had. The radiative corrections are the largest corrections which must be made. The error which would be introduced in ρ by neglecting these corrections would be to lower it by 0.04, when a fit is made for the region $0.3 \leq x \leq 0.95$. Above $x = 0.95$ the corrections become increasingly large and therefore this region of the spectrum provides a sensitive test of these corrections.

C. Modifications of the Theoretical Spectrum Introduced by the Measurement

Several additional corrections were made to the spectrum of Eq. (30) to account for some of the features of the experimental apparatus. Each of these corrections has the property that it cannot be accounted for on an event-by-event basis. To remove their effects from the experimental data would have required a difficult and tedious numerical solution of a set of integral equations, whereas the effects can be included in the theoretical spectrum by a direct numerical integration. These corrections were as follows:

1. Bremsstrahlung in the target counter, the first window of the vacuum chamber and spark chamber I.
2. Ionization loss in the first window of the vacuum tank, the wrapping of the target counter and the first spark chamber.

3. The effect of the finite resolution of the momentum measurement.

Most of the bremsstrahlung was generated in the target counter and it was the largest of the three corrections. Bremsstrahlung was treated in the limit of complete screening where γ, the screening parameter, is less than 1. If P is the energy of the photon, E_o the initial electron energy, and E the final energy, γ is given as

$$\gamma = \frac{100(M_e)}{(E+k)} \left(\frac{k}{E}\right) Z^{-1/3} \tag{31}$$

The cross section per unit energy of a photon of energy k in this approximation is

$$d\sigma = 4Z^2e^2r_o^2 \left(1 + \left(\frac{E}{E_o}\right)^2 - \frac{2}{3}\left(\frac{E}{E_o}\right)\right) \log\left(183\ Z^{-1/3}\right) \frac{dk}{k} \tag{32}$$

The probability that a positron will lose energy in the interval k to k+dk after passing through a thin piece of material is dW(k).

$$dW(k) = \left(\frac{N_o}{A}\right) \rho \ell d\sigma \ . \tag{33}$$

The effect of the finite thickness of the target counter was included by using the Bethe-Heitler formula[28] given in Eq. (34).

$W(b\ell, Y)$ is the probability that the positron would have an energy $E_o e^{-Y}$ or more after traversing a sample of thickness ℓ.

$$W(b\ell, y) = \frac{(b\ell-1, y)!}{\Gamma(b\ell)} \tag{34}$$

$$y = \ell n(E_o/(E_o-k)) \ .$$

If bremsstrahlung losses were ignored the observed value of ρ would have been lower by 0.007 than the actual value of ρ. The bremsstrahlung correction diverges at the endpoint. This like those in the inner bremsstrahlung, is an infrared divergence. Of some importance is the fact that the correction is very important for $x > 0.95$ and small below this region.

For positrons (or electrons) the average energy loss due to ionization is not the most probable energy loss and it is possible for a positron to lose all its energy in a single collision with an electron. Because there is a significant chance that a positron will lose several times the most probable energy loss, the detailed shape of the distribution of the energy losses must be taken into account.

The losses due to ionization in the target counter wrapping, Chamber I, and the first vacuum tank window were taken into account by using the Landau distribution.[29] If only the average energy loss in these materials had been considered and the shape of the probability distribution of energy losses had been ignored, the measured value of ρ would have been low by 0.002. Ionization losses in the active part of the target counter were corrected on an event-by-event basis.

The finite resolution of the spectrometer is accounted for by folding in a gaussian with a width consistent with the experimental resolution at the endpoint. It is not necessary to consider the momentum dependence of the resolution since the effect of finite resolution is important only within a few standard deviations of the maximum energy.

The theoretical spectrum which was compared with the experimental data is the sum of two parts. The first part is the spectrum for the case $\rho = 3/4$ and $\eta = 0$. This part is obtained by folding into Eq. (30) all the corrections discussed in Sec. V-C. The second part represents the difference between the spectrum for which $\eta \neq 0$ and $\rho = 3/4 + \Delta\rho$ and the spectrum for which $\rho = 3/4$ and $\eta = 0$. The difference of two spectra contains no interval radiative corrections but does include all other corrections discussed in this section. An important feature to be noted about the corrections made to the simple theory of Eq. (9) is that these made very large changes to the spectrum above $x = 0.95$. While it would be possible to get a good fit to experimental data for the momenta below this momentum, even if the corrections were ignored or made improperly, it would not be possible to get a good fit to the momenta above 0.95 unless the corrections were included and made properly. Thus, a good fit to experimental data over the whole momentum spectra is evidence for the validity of the corrections.

D. Bhabba Scattering in the Target and Positron Annihilation

No corrections were made to the theoretical spectrum to account for energy loss in the counter due to ionization, since the pulse height was used to correct each event in the experimental spectrum. The pulse height measured the positron energy loss correctly only when no secondary electrons had

escaped. Secondary electrons were produced when a positron transferred more than 0.2 MeV kinetic energy to an electron in the target. The following analysis shows that when a secondary electron was produced, the event was rejected either because the pulse height exceeded the maximum acceptable value (0.54 MeV) or a double spark occurred in Chamber I. The secondary electrons must have had at least 0.2 MeV kinetic energy to have escaped the target. If it had less energy it would always have been deflected back into the counter by the magnetic field. If it had an energy of more than 9 MeV, it would have made a double spark in Chamber I. There was a probability of 5% that a secondary electron would acquire a kinetic energy between these limits by positron-electron scattering. However, the probability it acquired this energy and emerged from the counter with at least 0.2 MeV is 0.5%. Of the electrons which escaped, 80% were either deflected back into the counter or caused a double spark in Chamber I. Electrons which made more than one traversal of the target counter had a pulse height which exceeded the maximum limit and the event associated with this electron was rejected. These two effects caused the rejection of more than 98% of the events which contained a secondary electron with a kinetic energy of more than 0.3 MeV; as a result no correction must be made for the events which were retained. There was a small momentum dependence of the fraction of the events rejected, and thus a small bias was made in the selection of events. This bias is considered along with other systematic errors in Sec. VII.

Positron annihilation in flight was not taken into consideration when the theoretical spectrum was made. When annihilation took place in the target counter, the spectrometer, or the E1 counter, there was no event trigger. The fraction of positrons which annihilated was about 1/2%. The number of annihilation events depends on the positron energy and hence a small correction must be made. The correction is made in Sec. VII.

VI. CONSTRUCTION OF THE EXPERIMENTAL SPECTRUM

A. Data Processing and Editing

The fact that 10^7 events had to be processed by a computer made it necessary to use data-processing techniques that are out of the ordinary routine encountered by physicists. FORTRAN because of its slowness in handling I/O and executing BCD-to-binary conversion was entirely unsuitable for the data processing. Four different machine language programs were written and the average time to run an event through all the programs was 15 msec. The programs can be separated into three categories according to their function, as follows:

1. Editing;
2. Geometric reconstruction of the trajectories;
3. Histogramming .

The programs are described briefly in the following paragraphs and in somewhat more detail in Appendix III.

a. Approximately 8% of the events had more than one missing spark and are therefore without any value.

b. Blocks of events could not be processed because of

occasional failures in the computing machinery of sonic spark chamber electronics.

c. The 7094 computer on which geometric reconstruction was done is a fixed word length binary computer, while the 1401 is a variable length word BCD computer.

For these three reasons, primarily the last, the raw data tapes, which were written by the 1401, were edited on the 7094 and rewritten in binary form. During the editing each input data record was checked for its form and its identity with the previous event. Events which had either the wrong form or which were identical with the previous event were rejected. Of the remainder of the events those which had no sparks missing were written on one binary output tape and those which had a single missing spark were written on a separate binary output tape. Approximately 6% of events had only one missing spark and these events were used solely to study spark chamber efficiency.

B. Geometric Reconstruction

After editing each event is reconstructed and the result is written on tape. The coordinate position of the spark within each chamber, x_i and y_i, are computed using Eqs. (22) and (23). The chamber coordinates are transformed to space coordinates of the coordinate system shown in Fig. 27.

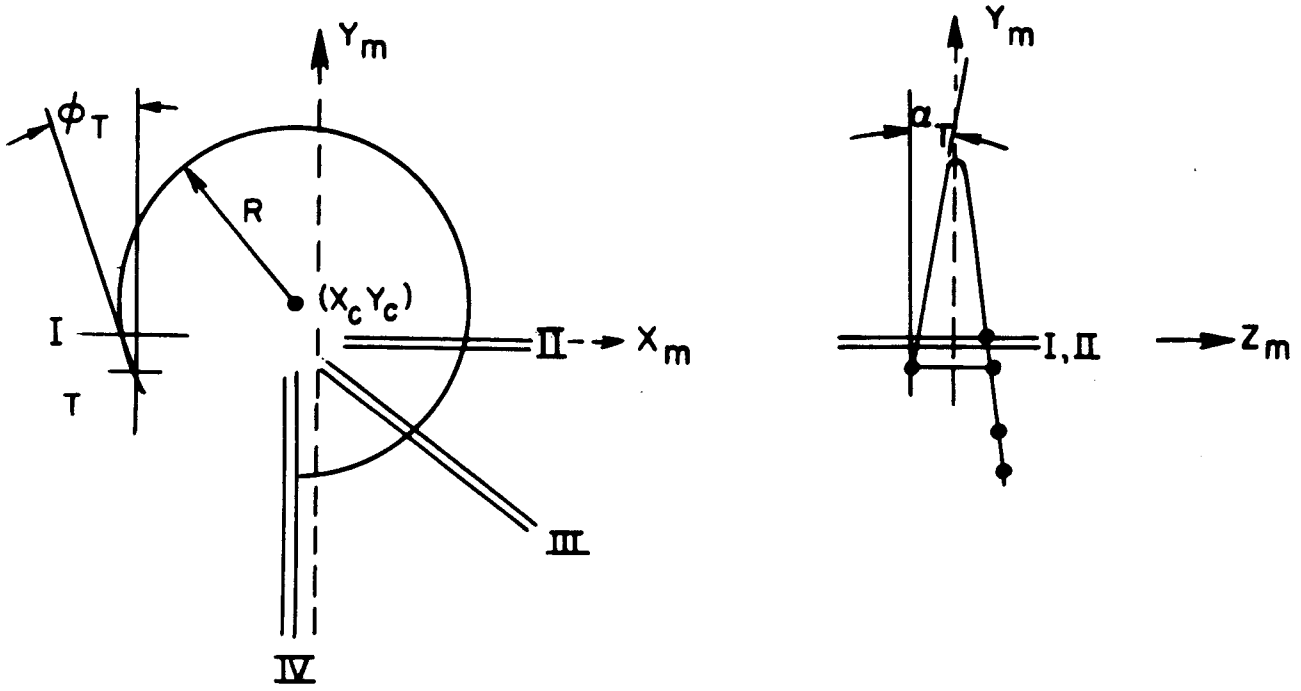

Fig. 27 Space Coordinates Used for Trajectory Reconstruction

z_m The coordinate axis which is parallel to the magnetic field.

x_m The coordinate axis which lies in the plane of the high voltage plate of Chamber II and is perpendicular to z_m. $x_m = 0$ is located at a point in Chamber II.

y_m The coordinate axis perpendicular to x_m and y_m, which lies in the plane midway between the pair of microphones 1 and 3 and the pair 2 and 4 in Chamber II.

x_c, y_c The center of the circle in the space coordinate system made by projecting the helical trajectory of the positron onto the x_m, y_m plane.

φ_T The angle made by Y_m with the tangent to the projected circle at its intersection with the target.

α_T The angle made by the tangent to the helix with the x_m, y_m plane at the target.

R The radius of the projected circle.

This figure also serves to define the angular coordinates, φ_T and α_T. A helix is fitted to the coordinates of the sparks in Chamber I and II and the x coordinate of Chamber III. This helix is projected into Chamber IV and the projected point is compared with the actual spark location. The difference between the projected trajectory and the actual spark location is used to eliminate the events in which the positron is scattered by the vacuum tank walls. There are three such differences; DZ3ACT, DZ4ACT, and DY4ACT; and they are the difference respectively between the projected and actual z coordinates in Chamber III and IV and the difference between the projected and real y coordinates in Chamber IV. The helix is corrected for the energy losses due to ionization in the material between the exit window of the vacuum tank and Chamber III. The principal effect of these losses is to cause an error in φ_T. The error in momentum due to these losses is proportional to $\sin\phi_I$; where ϕ_I is the azimuthal angle at Chamber I.

The momentum of the positron, when it emerges from the target counter, is computed from the radius of curvature and the mean magnetic field. No attempt was made to correct for field variations over a trajectory. The energy loss in the target due to ionization is corrected for by using the pulse height from the target counter. The relation between pulse height and the ionization loss was determined experimentally in the following manner. For each interval of pulse

height the location of the endpoint of the spectrum was determined. The relationship between pulse-height interval and the shift in the endpoint was found to be linear for all statistically significant intervals of pulse height. The range of statistically significant intervals of pulse height spanned a shift of the endpoint of 0.7 MeV. This is approximately one and a half times the most probable energy loss for a positron traversing the full thickness of the counter. The results of this analysis are shown in Fig. 16. The endpoint in each case was defined as the momentum at which the population of the histogram was half the value of the population at 51.5 MeV/c.

DZ3ACT, DZ4ACT, and DR4ACT have gaussian distributions, the widths of which are functions of P and ϕ_T. DZ3ACT is due principally to multiple scattering, in the vacuum tank windows and spark chamber II. The scattering by a thin foil can be written as

$$\left\langle (\Delta X)^2 \right\rangle^{1/2} = \frac{\ell_p}{p\beta} f(t, t_o) \qquad (35)$$

ΔX is the displacement of a track due to a scattering by a material of thickness, t, and radiation length, t_o, ℓ_p is the path length of the track after the scattering. This can be applied to DZ3ACT by taking ℓ_p to be

$$\ell_p = P \left(\frac{dR}{dP}\right) \phi_{23} \qquad (36)$$

where ϕ_{23} is the arc subtended by the trajectory in going from Chamber II to Chamber III. Equation (35) can be written for positrons with small dip angles as

$$\left\langle (\text{DZ3ACT})^2 \right\rangle^{1/2} = \frac{dR}{dP}\, \phi_{23}\, f(t) \ . \tag{37}$$

ϕ_{23} depends rather strongly on momentum. Since DZ3ACT is used as a criterion to distinguish between multiple scattering in the foils and scattering of the vacuum tank walls, the momentum dependence of ϕ_{23} must be factored out. If it is not done, the selection on DZ3 will introduce a bias favoring low momentum. The momentum dependence is eliminated by dividing by ϕ_{23}. To define

$$\text{DZ3} = \left(\frac{dP}{dR}\right) \frac{\text{DZ3ACT}}{\phi_{23}} \tag{38}$$

dP/dR is retained to make it possible to use one criterion for all fields. When scattering in the gas is considered, t also depends on ℓ_p and a more complicated correction is made to include this effect and to correct for the fact that ℓ_p for the vacuum tank is not $R\varphi_{23}$. In a similar way DZ4ACT and DY4ACT are modified to give momentum independent descriptions of the multiple scattering. Histograms of these variables are shown in Figs. 28 and 29.

In addition to computing the dip angle, α, a new variable α' is introduced for the purpose of making histograms. At each point on the target counter the maximum useful range of α is 12°. This is the range of α within which all events in a selected range of ϕ and p are accepted by the spectrometer. The center of this range depends on the location in the target. In order to select the largest possible sample of events the variable α' which is defined by Eq. (39) is used in the selection criteria.

$$\alpha' = \alpha - \frac{Z_T}{125 \text{ cm}} \qquad (39)$$

By selecting events from a fixed region of α', each part of the target has a different solid angle, but this solid angle does not depend on momentum. A factor of two increase in useful data is obtained by this means.

After calculation, each event is truncated and written on tape at 250 events per record. Table VII gives a list of those events which are written on the "P tape" and the number bits assigned to each variable.

TABLE VII

Information Retained After Reconstruction

Variable	Range	Bits	Variable	Range	Bits
p	15 to 55 MeV	12	$(D1234)_{II}$	0 to 8×10^5 t^2	6
φ_T	-30^o to $+50^o$	9	$(D1234)_{III}$	0 to 8×10^5 t^2	6
α_T	-20^o to $+20^o$	9	$(D1234)_{IV}$	0 to 8×10^5 t^2	6
α'_T	-20^o to $+20^o$	9	XI		6
X_T	-4 to +4 cm	6	YI		6
Z_T	-4 to +4 cm	6	XII		6
DZ3	-2 to +2 MeV/c	6	YII		6
DZ4	-2 to +2 MeV/c	6	XIII		6
DR4	-2 to +2 MeV/c	6	YIII		6
PHI	0 to 1600	7	XIV		6
PH2	0 to 9999	5	YIV		6
$(D1234)_I$	0 to 4×10^5 t^2	6	Identification		12

If an event does not fall into the range given in Table VII, it is tested to see whether it falls in a range which is twice as large, and if the event is within the new range it is written onto a separate tape, the "rejected P tape". Events which do not fall within the enlarged range are discarded and a record is kept of the number of such events. Approximately 90% of the edited events are accepted for the "P tape".

At this stage the number of tapes is still too large to construct histograms without a prohibitive amount of time being used on the 7094. Therefore, the "P tapes" were edited by reducing the number of significant figures carried in each variable and by reducing the number of variables to 11. The P' tape, the result of this editing, is the tape from which the histograms are constructed. A description of the P' tape is given in Appendix III.

C. Selection of Events for the Experimental Spectrum

A partial selection of events is made at each stage of the computations. Events with missing sparks are rejected during the data-tape editing. During the geometric reconstruction, events which had double sparks in any chamber or which had sparks within 1/4-in. of the steel frame of the spark chamber plates were rejected. The double spark criteria were that D1234 could not exceed 4×10^5 in Chamber I, and 8×10^5 in Chamber II, III, IV. The units are $(0.2\ \mu\text{sec})^2$. These values correspond to an ambiguity of position of 1 cm.

The next criteria which were imposed on the acceptable events were the limits of pulse height in the target counter.

The pulse height had to be at least 0.05 MeV of energy loss, which was somewhat larger than single photoelectron noise. The pulse height had to be less than 0.54 MeV. This upper limit helped to eliminate events due to spurious beam particles passing through the target counter and a large fraction of the events in which an energetic secondary δ ray was produced. The upper cutoff was well within the limit of linearity in the pulse height analysis. The upper cutoff introduces a momentum dependent bias which is accounted for in Sec. VII.

After making a preliminary estimate of the useful regions of ϕ_T and α', the histograms of DZ3, DZ4, and DR4 were constructed for each 5 MeV/c band of momenta. In addition, the events in these histograms were within the same maximum limits on all other variables which were imposed when the final selection was made. Some of these histograms are shown in Figs. 28 and 29. The distributions are gaussian and their widths are not dependent on momentum, as can be seen from Fig. 30. The events in the tails of these distributions contain the positrons which scattered off obstructions or muons which after scattering in the target counter, were detected in the E counter.

The spatial extent of the scattering permitted by the limits depends on momentum, as has been discussed in Sec. VI-B. At 50 MeV/c the limits of acceptable DZ3 and DR4 correspond to a scattering of $\pm$ 2.5mm, and the limits for DZ4 correspond to a scattering of $\pm$ 5.0mm. Since the histograms for these variables are gaussian, the fraction of good events which were rejected can be estimated. Less than 0.1% of the good events

were rejected by the DZ4 limits and hence no bias was introduced by these limits. Of the good events 1% were outside the limits of DR4. The momentum dependence of the fraction of these events was less than 10% and as a result a negligible bias was introduced by this selection. The momentum dependence of the widths of the DR4 distributions is shown in Fig. 30. The limits on DZ3 gave a 4% rejection of good events. The fraction of good events rejected by this criterion was not dependent on momentum, as the shape of the DZ3 distribution did not depend on momentum. The purpose of the limits on DZ3, DZ4, and DR4 was to eliminate events in which the positron scattered off an obstruction and lost some of its energy. A small contamination of events which did this remains and is discussed in Sec. VII-F. The pulse height criteria rejected 5% of the events, as did the scattering criteria.

The next selection chose events from a region of α' and ϕ_T, such that the momentum dependence of the spectrum did not depend on the choice of the region of α' and ϕ_T. The size of this region was determined from the data and is in agreement with the expected region. Histograms of α' were made for each 5.0 MeV/c interval of momentum, and each 11^o interval of ϕ_T, and each cm of the target along the Z_T direction. The α' histograms are constant for a symmetric range of α' and fall to zero within a fraction of a degree. Plots of two such histograms which have been summed over Z_T are shown in Fig. 31. As can be seen from the histogram the minimum interval

of α' over which the population is constant occurs at the maximum momentum. As the width of the interval varies inversely with the momentum, an unbiased selection of events is made when all the events which lie within the interval defined by the maximum momentum are chosen. The width of this interval is 11.5° and is symmetric at about zero.

After determining the maximum useful region of α', histograms of φ_T were constructed for events satisfying $|\alpha'| < 5.75^{\circ}$ and for each 5 MeV/c band of momenta. As with α' the maximum useful region of φ_T is that region of φ_T for which the histogram population is constant for all values of P. The region depends on the choice of the ratio of the minimum to maximum momentum of the final momentum selection. For a ratio of 0.65, the useful range of φ_T is $-19^{\circ} \leq \varphi_r \leq 18.5^{\circ}$. Figure 32 shows the φ_T histograms for each 5 MeV/c band of momenta for the 6.6 kG field case and the cutoff criteria. Unlike the α' histograms the distributions do not have a sharp cutoff, but have a gradual decrease for large φ_T. The histogram for the region 50.0 MeV/c to cutoff is not flat anywhere and changes by 6% over the useful region. The latter effect is caused by the variation of the magnetic field at large radii, together with the fact that this momentum band contains the endpoint. At $\varphi_T = 18.5^{\circ}$ and P = 50 MeV/c the momenta will be measured by 1/4% due to the field. As a result the element of population between 50 MeV/c and 50.08 MeV/c will be found in the band between 45 MeV/c and 50 MeV/c.